

Average Calibration Losses for Reliable Uncertainty in Medical Image Segmentation

Theodore Barfoot¹, Luis C. Garcia-Peraza-Herrera¹, Samet Akcay², Ben Glocker³, and Tom Vercauteren¹

¹King’s College London (theodore.d.barfoot@kcl.ac.uk)

²Intel Corporation

³Imperial College London

Abstract

Deep neural networks for medical image segmentation are often overconfident, compromising both reliability and clinical utility. In this work, we propose differentiable formulations of marginal L1 Average Calibration Error (mL1-ACE) as an auxiliary loss that can be computed on a per-image basis. We compare both hard- and soft-binning approaches to directly improve pixel-wise calibration. Our experiments on four datasets (ACDC, AMOS, KiTS, BraTS) demonstrate that incorporating mL1-ACE significantly reduces calibration errors, particularly Average Calibration Error (ACE) and Maximum Calibration Error (MCE), while largely maintaining high Dice Similarity Coefficients (DSCs). We find that the soft-binned variant yields the greatest improvements in calibration, over the Dice plus cross-entropy loss baseline, but often compromises segmentation performance, with hard-binned mL1-ACE maintaining segmentation performance, albeit with weaker calibration improvement. To gain further insight into calibration performance and its variability across an imaging dataset, we introduce dataset reliability histograms, an aggregation of per-image reliability diagrams. The resulting analysis highlights improved alignment between predicted confidences and true accuracies. Overall, our approach not only enhances the trustworthiness of segmentation predictions but also shows potential for safer integration of deep learning methods into clinical workflows. We share our code here: <https://github.com/cai4cai/Average-Calibration-Losses>

Keywords: Semantic, Segmentation, Calibration, Loss, Confidence, Reliability, Uncertainty

1 Introduction

Deep neural networks (DNNs) often exhibit *miscalibration*, meaning their predicted probabilities (confidence) do not reflect true outcome likelihoods (accuracy). In practice, DNNs tend to be overconfident, especially when trained on limited data, as is common in medical imaging tasks [14, 27]. In the safety-critical domains of medical diagnosis and segmentation, this miscalibration poses serious risks. A model might assign high confidence to an incorrect decision, misleading clinicians. Conversely, well-calibrated models improve the *trustworthiness* of AI predictions by aligning predictive confidence with accuracy [10, 14]. Better-calibrated models can support improved clinical decisions and patient outcomes. For example, in radiotherapy planning, accurate confidence estimates help doctors identify uncertain regions in need of review [6]. Overall, calibration of DNNs is emerging as a key requirement for reliable deployment of AI in healthcare.

Historically, calibration has primarily been addressed using post-hoc methods. Techniques like Platt scaling and temperature scaling (TS) apply simple corrections to a model’s predictions after training [14]. These approaches have limitations:

they fail to leverage the model’s full capacity to learn calibration directly, and they usually employ global adjustments, unable to correct instance- or class-specific calibration errors.

To address this, we propose integrating calibration directly into the model’s training (train-time calibration), enabling the network to intrinsically produce well-calibrated predictions without post-hoc adjustments. Our method specifically employs the Average Calibration Error (ACE) as both a calibration metric and a differentiable auxiliary loss function. Unlike the widely used Expected Calibration Error (ECE), which weights errors by bin population and is dominated by highly confident predictions [6], ACE treats all confidence ranges equally [35]. This uniform treatment is particularly important for medical segmentation tasks, where uncertain predictions often occur at clinically critical regions like tissue boundaries.

Calibration metrics traditionally rely on dataset-level statistics. For classification tasks, this can lead to inefficient estimation from small mini-batches [23, 25]. However, segmentation outputs voxel-level predictions per image, inherently providing ample data for stable calibration estimates even from single images. Exploiting this fact, we introduce a straightforward, differentiable ACE-based loss using standard probability binning operations, circumventing the need for soft relaxations or proxy losses [19, 22].

To better understand calibration performance across image

segmentation datasets, we introduce *dataset reliability histograms*, an aggregation of per-image reliability diagrams. These histograms provide a comprehensive tool to visualise the calibration of a predictor over an entire dataset.

This work significantly extends our previous conference publication [3]. Specifically, we pair our marginal L1-ACE (mL1-ACE) auxiliary loss with a popular segmentation loss combination: Dice Similarity Coefficient (DSC) plus Cross-Entropy (CE), which generally yields better-calibrated predictions than DSC or CE alone [26]. We also extend mL1-ACE with a soft-binning approach, providing smoother gradients during training, and evaluate our method comprehensively on additional datasets.

Our results show that incorporating mL1-ACE (both hard- and soft-binned) significantly reduces calibration errors compared to the baseline DSC+CE loss. We evaluate calibration errors using both micro- and macro-averaging, and segmentation performance via DSC. While soft-binned mL1-ACE (sL1-ACE) achieves greater calibration improvements, it can slightly compromise segmentation accuracy. In contrast, hard-binned mL1-ACE (hL1-ACE) notably improves calibration while largely maintaining segmentation performance.

In summary, we propose *mL1-ACE*, a differentiable calibration loss for semantic segmentation derived from marginal reliability diagrams. Unlike previous classification-focused approaches, we leverage dense voxel-level predictions to efficiently compute calibration metrics per image. Our method, evaluated on four public datasets, demonstrates the effectiveness of both binning strategies and introduces dataset reliability histograms for visualising large-scale calibration trends.

2 Background and Related Work

2.1 Uncertainty Estimation in Medical Segmentation

Uncertainty in image segmentation predictions is commonly divided into *aleatoric* (data-related) and *epistemic* (model-related) uncertainty [20]. Several methods have been proposed to model these uncertainties. Epistemic uncertainty is often estimated using *Monte Carlo dropout* [13] or *deep ensembles* [24], while aleatoric uncertainty can be modelled by predicting per-voxel variances [20] or through *test-time augmentation* [1]. More expressive probabilistic segmentation networks, such as the *Probabilistic U-Net* [21] and *PHiSeg* [4], model a distribution over possible segmentations. *Stochastic Segmentation Networks (SSNs)* [29] extend this by modelling spatially correlated aleatoric uncertainty, enabling the generation of coherent, plausible segmentation variants. The QU-BraTS challenge [28], part of the BraTS 2020 benchmark, provided a platform for evaluating these methods in brain tumour segmentation. Top-performing entries combined dropout, test-time augmentation, and ensembles to estimate voxel-level uncertainty and demonstrated that capturing both epistemic and aleatoric components improves calibration and reliability in medical segmentation tasks. Nonetheless, in the majority of

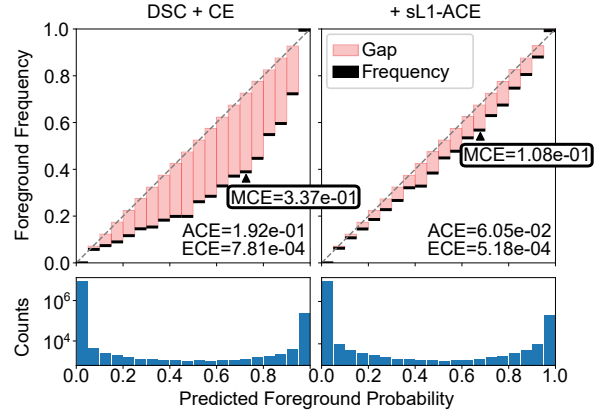


Figure 1: Reliability diagrams for BraTS 2021 (case 00095, whole tumour class), comparing baseline DSC plus CE loss (left) and baseline plus our auxiliary soft-binned mL1-ACE (sL1-ACE) loss (right). Each diagram shows empirical foreground frequency (accuracy) versus predicted foreground probability (confidence), voxel counts per bin, and associated calibration errors (ACE, ECE, MCE). The additional sL1-ACE loss substantially reduces the baseline model’s overconfidence.

previous medical image segmentation works, little emphasis has been put in principled uncertainty estimation and calibration, and the need to consolidate uncertainty estimation towards established metrics.

2.2 Reliability Diagrams and Calibration Metrics

Reliability diagrams are a standard tool for visualising model calibration. An example of such is shown in Fig. 1. They plot the actual accuracy achieved against the model predicted probability (confidence) for samples at that confidence level [11]. To construct a reliability diagram, predicted class probabilities are discretised into bins. For each bin, one computes the *average confidence* of predictions in the bin (which will be close to the bin centre value) and the *actual proportion* of those predictions that were correct. The difference between the confidence and accuracy (DCA) in each bin is the calibration error for that bin. A perfectly calibrated model would have zero difference for every bin. In the context of classification tasks, a reliability diagram is typically constructed for a dataset. However, in semantic segmentation, the output space is much larger, with each pixel/voxel representing a separate prediction. This permits the construction of a reliability diagram for each image, meaning that derived calibration error metrics can be calculated on a per-image basis. To the best of our knowledge, this observation has not been exploited in previous work.

Several scalar metrics distil calibration performance into a single number. The most widely used is the Expected Calibration Error (ECE), which is a weighted average of the per-bin DCA, where the weights are the number of samples in each bin [35]. By contrast, the *Average Calibration Error*

(ACE) weights each bin equally by simply averaging the per-bin gaps [34]. The *Maximum Calibration Error (MCE)* is another metric that reports the worst-case bin error [35]. Additional metrics, such as the Brier Score [8] and Overconfidence Error (OE) [40], have also been employed. Most calibration metrics assess marginal or top-label calibration by evaluating each class independently. In contrast, *canonical* calibration requires that the predicted probability vector as a whole is calibrated with respect to the true class distribution. This is more stringent and challenging to evaluate, especially in high-dimensional settings like segmentation. Popordanoska et al. [37] addressed canonical calibration in classification by proposing a consistent and differentiable L_p calibration error estimator based on Dirichlet kernel density estimation, enabling scalable, distribution-level calibration assessment. While canonical calibration may offer insight beyond marginal calibration, it is beyond the scope of this work.

2.3 Post-hoc Calibration Techniques

One approach to mitigating DNN miscalibration is to address it after training in a post-hoc fashion, without modifying network weights. A common approach is Temperature Scaling (TS) [14, 36], which multiplies logits by a scalar temperature to soften (temperature > 1) or sharpen (temperature < 1) predicted probabilities, and can be applied globally or per-class in segmentation tasks. Other methods include Platt scaling, isotonic regression, beta calibration, and Dirichlet calibration, with recent spatially aware extensions leveraging local neighbourhood information to further improve calibration [38]. These methods provide a means to improve calibration, without affecting the accuracy of the predictor, but very few parameters are leveraged for this calibration, limiting the ability to provide context-aware and instance-specific calibration.

2.4 Augmentation for Train-time Calibration

An alternative to post-hoc calibration is *train-time calibration* techniques, which leverages the high parameter count of DNN networks to achieve calibration. This can be performed indirectly, with techniques such as *label smoothing*, which softens hard one-hot labels, have been shown to reduce overconfidence and thereby improve calibration [39]. Additionally, data augmentation strategies, such as mixup [40, 43], also contribute to model calibration by forcing the network to produce softer, more uncertain outputs on interpolated samples. These methods modify the ground truth used in the optimisation process to mitigate overconfidence issues but they lack control over the actual calibration performance.

2.5 Auxiliary Calibration Losses in Classification

A direct approach to improve model calibration is to modify the training objective by incorporating an auxiliary loss that explicitly targets calibration. In image classification, several

calibration-aware auxiliary losses have been proposed. For instance, Liang et al. [25] introduced a loss term based on the discrepancy between the predicted probabilities and the empirical accuracy (derived from the expected calibration error, ECE), penalising the model when reductions in the cross-entropy loss do not yield corresponding improvements in accuracy. According to Hebbalaguppe et al. [15], this DCA-based loss is purportedly limited by differentiability issues arising from discontinuities of the accuracy term due to the reliance on hard binning. To address this potential issue, Hebbalaguppe et al. [15] proposed the Multi-class DCA (MDCA) loss, which computes the calibration error by averaging over each class within a mini-batch rather than within fixed confidence bins. Moreover, Kumar et al. [23] introduced the Maximum Mean Calibration Error (MMCE) loss, a differentiable formulation that can be optimised jointly with the primary task. Other works have explored differentiable accuracy versus uncertainty calibration (AvUC) losses [22] and soft calibration objectives (S-AvUC) that employ continuous binning to produce differentiable estimates [19]. Recently, Boddal et al. [7] developed a differentiable surrogate for expected calibration error (DECE) using soft binning and smooth approximations, although its reliance on meta-learning increases complexity and may limit wider applicability. As mentioned above, auxiliary losses have also been extended to canonical calibration [37]. Recent uncertainty-aware training strategies in medical image classification demonstrate that incorporating calibration-related loss terms can reduce miscalibration by a substantial margin while maintaining (or even improving) accuracy [10]. Dawood et al. showed that a *Confidence Weight* loss penalty on incorrect high-confidence predictions reduced the expected calibration error by 17–22% in cardiac MRI classification tasks, with slight accuracy gains.

The approach of auxiliary calibration losses has significant limitations in the context of image classification due to the small output space, as each input image only has one associated prediction and therefore a single confidence value and a binary accuracy term. This can be alleviated by using a larger mini-batch, but this is limited due to large input images, hence why proxy calibration objectives or efficient sampling methods have to be employed.

2.6 Auxiliary Calibration Losses in Segmentation

In contrast to classification problems, segmentation tasks produce dense, per-pixel/voxel predictions, yielding a much larger number of confidence estimates per image. This can make calibration during mini-batch optimisation more effective, as the larger number of samples provides more stable and statistically meaningful estimates of calibration error for each forward pass. The use of auxiliary calibration losses in semantic segmentation is less common than in classification, yet it is equally critical in medical imaging applications. Standard segmentation losses, such as the Dice loss, have been shown to produce overconfident predictions [27], despite their effectiveness in handling class imbalance. To address this,

Yeung et al. [42] proposed the DSC++ loss, which modifies the Dice loss by adjusting false positive and false negative penalties according to class frequency. Similarly, Neighbour-Aware Calibration (NACL) methods [30, 31] incorporate spatial consistency by penalising overconfident predictions in local neighbourhoods. Despite reported reduction in overconfidence with these approaches, there remains a need for a more controlled approach to ensure that model confidence estimates align more closely with observed accuracy while maintaining high segmentation performance.

3 Method

3.1 Reliability Diagrams and Dataset Reliability Histograms

Reliability diagrams are constructed by discretising model predictions into probability bins and comparing the average predicted probability within each bin against the observed empirical frequency of that class. An illustrative example of a reliability diagram is provided in Fig. 1. We make the observation that in semantic segmentation, due to the highly dimensional prediction space, calibration errors can be computed on a per-image basis. In our primary formulation, for each image and for each class c , the predicted probability space is discretised into M bins using a hard-binning approach. Then, for each bin m , we compute the expected foreground probability e_m^c and the observed foreground frequency o_m^c . The difference between these two quantities represents the difference between confidence and accuracy (DCA) in a marginal, class-wise context. More formally, we define:

$$o_m^c = \mathbb{E}[\mathbf{Y}_i^c | i \in B_m^c], \quad e_m^c = \mathbb{E}[f_\theta(\mathbf{X})_i^c | i \in B_m^c], \quad (1)$$

where \mathbf{X} is the input image, or dataset (for micro-average metrics), \mathbf{Y} the associated ground truth label-map, B_m^c denotes the set of voxels i in the image whose predicted probability for class c falls into bin m , and f_θ is our predictor (typically a ConvNet) with trainable weights θ .

This approach can trivially be applied across all voxels in the dataset (micro-averaging) to produce a reliability diagram for the dataset. However, as we are able to construct reliability diagrams per-image, we can leverage these to then construct a *dataset reliability histogram* (rather than diagram). This enables more fine-grained analysis of calibration performance across the dataset. We start by collecting all $(e_m^c; o_m^c)$ pairs for all images. For each bin m , by construction, the e_m^c values across the images will be close to the centre of B_m^c . The image-specific o_m^c values, however, can vary significantly within each bin m . To get insight in the corresponding distribution, we compute the histogram of image-specific o_m^c values within each bin m . The resulting dataset reliability histogram is visualised in 2D by plotting, for each m bin along the horizontal axis, the 1D histograms of o_m^c values along the vertical axis. As illustrated in Fig. 4, this provides an intuitive visualisation of calibration variability across the entire dataset.

3.2 Micro- and Macro-Averaged Calibration Metrics

We use the sum of absolute differences between e_m^c and o_m^c , which we refer to as L1 differences, as the basis of our calibration metrics:

$$\text{mL1-ECE} = \frac{1}{C} \sum_{c=1}^C \sum_{m=1}^M \frac{n_m^c}{N} |o_m^c - e_m^c|, \quad (2)$$

$$\text{mL1-ACE} = \frac{1}{CM} \sum_{c=1}^C \sum_{m=1}^M |o_m^c - e_m^c|, \quad (3)$$

$$\text{mL1-MCE} = \frac{1}{C} \sum_{c=1}^C \max_m |o_m^c - e_m^c|, \quad (4)$$

where n_m^c is the number of voxels in bin B_m^c , C the number of classes, and N is the total number of voxels.

In our preliminary work [3], these calibration metrics were computed per image (macro-averaging) and then averaged over the dataset. Here, we additionally perform micro-averaging, aggregating predictions across all images. Specifically, aggregated foreground probabilities are simple averages, observed frequencies are bin-count weighted averages, and bin counts are summed directly. In our implementation, this aggregation is performed on-the-fly without storing the entire output tensor in memory, ensuring efficiency even for large datasets.

3.3 Hard- and Soft-Binned ACE Loss Functions

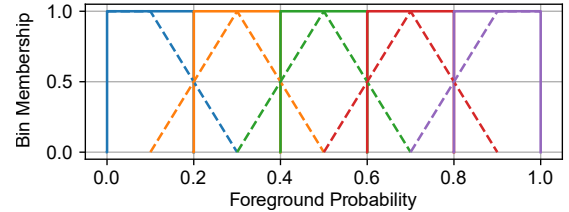


Figure 2: Visualisation of hard- (solid line) and soft- (dashed line) foreground probability binning assignment functions for 5 bins.

For training, we employ the marginal L1 Average Calibration Error (mL1-ACE) loss defined in (3) in two variants: hard- and soft-binning, which we also refer to as hL1-ACE and sL1-ACE, respectively. In this formulation, we define a *membership function* $\psi_m(x)$ that assigns a weight to a prediction x for bin m , as shown in Fig. 2. As is typical with kernel density estimation, the choice of kernel determines the nature of the binning.

Hard-Binning (Square Kernel): For hard-binning, the membership function is a square wave:

$$\psi_m^{\text{hard}}(x) = \begin{cases} 1, & \text{if } x \in [b_{m-1}, b_m), \\ 0, & \text{otherwise,} \end{cases}$$

where b_0, b_1, \dots, b_M are the bin boundaries defined by a uniform partition of the interval $[0, 1]$; that is,

$$b_k = \frac{k}{M}, \quad k = 0, 1, \dots, M.$$

Soft Binning (Triangular Kernel): For soft-binning, we define a triangular kernel centred at the midpoint of each bin. The membership function for bin m is:

$$\psi_m^{\text{soft}}(x) = \begin{cases} 1, & \text{if } m = 1 \text{ and } x < \beta_1, \\ 1 - M \cdot |x - \beta_m|, & \text{if } \beta_{m-1} \leq x \leq \beta_{m+1}, \\ 1, & \text{if } m = M \text{ and } x > \beta_M, \\ 0, & \text{otherwise,} \end{cases}$$

where $\beta_m = \frac{b_{m-1} + b_m}{2}$ is the centre of bin m . Each triangular kernel peaks at 1 in its bin centre β_m , decays linearly to 0 at the adjacent bin centres β_{m-1} and β_{m+1} , and reaches 0.5 at the bin edges b_{m-1} and b_m .

Then, for class c , the expected foreground probability and observed foreground frequency are defined as

$$e_m^c = \frac{\sum_{i \in B_m^c} \psi_m(x_i^c) x_i^c}{\sum_{i \in B_m^c} \psi_m(x_i^c)}, \quad (5)$$

$$o_m^c = \frac{\sum_{i \in B_m^c} \psi_m(x_i^c) Y_i^c}{\sum_{i \in B_m^c} \psi_m(x_i^c)}, \quad (6)$$

where Y_i^c is the ground truth indicator for class c and x_i^c is the predicted probability for class c at voxel i . By adopting a kernel density estimation perspective, our method can easily be extended from using a square kernel (hard-binning), to a triangular kernel (soft-binning), or to any other suitable kernel (e.g. Spline, Gaussian, etc.) to compute voxel-level membership functions.

4 Experiments

4.1 Datasets

We evaluate our auxiliary calibration losses on four public medical image segmentation datasets: (1) **ACDC 2017** – the Automatic Cardiac Diagnosis Challenge Dataset [5], a cardiac MRI dataset with left- and right-ventricle and myocardium segmentation classes; (2) **AMOS 2022** – the large-scale Abdominal Multi-Organ Benchmark for Versatile Medical Image Segmentation [18], an abdominal CT and MRI dataset with 15 organ classes, from which only the CT images were used; (3) **BraTS 2021** – the Multimodal Brain Tumour Segmentation Benchmark dataset [2], a multimodal neurological MRI dataset with three tumour classes; and (4) **KiTS 2023** – the 2023 Kidney and Kidney Tumor Segmentation Challenge [16], a CT with semantic classes for kidneys, renal tumours and renal cysts. The ACDC, AMOS and KiTS datasets were chosen due to their reported suitability for benchmarking segmentation methods [17], while BraTS 2021 was included as it is widely used (including our previous work [3]).

The ACDC dataset provides separate training and testing datasets, with 100 cases in the training dataset and 50 cases in the testing dataset. A training-validation split of 90:10 was used, and the testing dataset was used as provided. For AMOS, only the CT images were used. The training dataset of 240 CT images was then split into training and validation with a ratio of 216:24. The validation dataset was used as the testing dataset, as the testing dataset is not publicly available. For the BraTS dataset, the publicly available training dataset of 1251 cases was split into training, validation and testing with a ratio of 1000:51:200 cases, using the same testing split as our previous work [3]. For KiTS, the training dataset of 489 cases was partitioned into training, validation and testing with a ratio of 352:39:98.

Of note for evaluation, the AMOS testing set has 13% of cases missing organs (e.g. gallbladder or prostate/uterus) due to field-of-view variation; BraTS has 4% of cases lacking necrotic or enhancing tumour labels; and over half (56%) of KiTS cases omit the cyst class.

4.2 Training and Evaluation

All training and evaluation was implemented via the MONAI framework [9]. Our open-source code can be found at <https://github.com/cai4cai/Average-Calibration-Losses>. A SegResNet model [32] was used, with 32 initial filters and 4 deep supervision layers, as employed by the KiTS 2023 competition winner [33]. We used the AdamW optimizer with a learning rate of 1×10^{-4} , 2×10^{-4} for AMOS, and weight decay of 1×10^{-5} . A warmup cosine scheduler was used, with a linear warmup period of 2 epochs with a warmup multiplier of 0.50, followed by cosine annealing for the remaining epochs. Training was run for 600 epochs for the ACDC and AMOS datasets and 1250 epochs for the BraTS and KiTS datasets. Validation was performed every 10 epochs, with the best model saved based on the validation Dice score. A fixed batch size of 2 was used, with the patch size maximised to fit within the GPU memory. All experiments were performed using an NVidia DGX cluster with V100 (32GB) and A100 (40GB) GPUs.

For the BraTS 2021 dataset, the same data augmentation preprocessing steps were applied as in [12]. For the remaining datasets, a minimal preprocessing pipeline was used, consisting of random foreground cropping, resampling, random affine transformations and intensity normalisation.

For each dataset, three models were trained: (1) a baseline model using a Dice plus cross-entropy loss with a weight ratio of 1:1; (2) a model incorporating the baseline loss with an additional hard-binned auxiliary mL1-ACE loss (hL1-ACE), maintaining a ratio of 1:1:1 for Dice, cross-entropy, and ACE losses; and (3) a model incorporating the baseline loss with an additional soft-binned mL1-ACE loss (sL1-ACE), also maintaining a ratio of 1:1:1. For the auxiliary calibration losses, 20 bins were used to discretise the foreground probability space. For any classes with no ground truth present, the mL1-ACE loss was set to zero during optimisation.

The saved model with the highest validation Dice score was used for evaluation on the testing dataset. The Dice score, Average Calibration Error (ACE), Expected Calibration Error (ECE), and Maximum Calibration Error (MCE) were computed for each model, using both micro- and macro-averaging. For all calibration metrics, a fixed number of 20 bins was used, with hard-binning of predicted foreground probabilities. Additionally, reliability diagrams were generated for each testing case and a dataset reliability histogram for the whole dataset.

5 Results

We report results, averaged across classes, excluding background, and for BraTS and KiTS we report the average of the hierarchical evaluation classes (HEC). HECs reflect the labels used clinically and group together sub-regions into a larger class, such as whole tumour for BraTS, to create nested or composite labels. We evaluate the performance of the baseline model, trained with DSC and cross-entropy (CE), against models trained with mL1-ACE auxiliary losses, with both hard and soft binning. We compare the models across four datasets: ACDC, AMOS, BraTS, and KiTS. We achieve a Dice score of 0.880 on ACDC, 0.883 on AMOS, 0.905 on BraTS, and 0.859 on KiTS with the baseline model. This can be compared to state-of-the-art values of 0.927, 0.897, 0.915 and 0.887, respectively, as reported in the literature [17].

5.1 Tabular Results

We find that both hard- and soft-binned mL1-ACE outperform the baseline in terms of macro- and micro-averaged ACE and MCE across all datasets. In general, both variants are able to maintain DSC performance across datasets, though in some cases this may vary slightly. Notably, soft-binned mL1-ACE outperforms both hard-binned mL1-ACE and the baseline in terms of macro-averaged ACE (Table 1). Specifically, soft mL1-ACE improves macro-averaged ACE by 40% on ACDC, 19% on AMOS 30% on BraTS and 36% on KiTS compared to the baseline. For micro-averaged ACE, soft mL1-ACE provides improvements of 66% on ACDC, 52% on AMOS, and 58% on BraTS. However, on KiTS, hard-binned mL1-ACE achieves the largest improvement, with a 23% enhancement over the baseline, as shown in Table 1. For ACDC, statistically significant improvements ($p < 0.01$) are observed in macro-ACE, macro-ECE, and macro-MCE when comparing the baseline to both variants; DSC is significantly lower only for soft mL1-ACE. For the AMOS dataset, macro-ACE and MCE are improved significantly ($p < 0.05$) by both mL1-ACE variants, with soft mL1-ACE showing the most significant improvements. While the reduction in DSC, due to the introduction of the auxiliary loss functions, is small it is still statistically significant ($p < 0.01$). There is no statistically significant reduction in ECE for either mL1-ACE variant. For BraTS, both calibration metrics macro-ACE and macro-MCE show significant differences ($p < 0.01$) for both hard and soft L1-ACE compared to the baseline; DSC is significantly decreased only with

soft mL1-ACE. For KiTS, similar to the ACDC dataset, statistically significant improvements ($p < 0.01$) in macro-ACE and macro-MCE are observed for both mL1-ACE variants. In this case, no significant differences in DSC or macro-ECE are observed.

5.2 Radar Plots

These observations are further supported by the normalised radar plots in Fig. 3, which show that both mL1-ACE variants are able to reduce calibration errors while largely maintaining DSC performance across all datasets. The exception to this pattern is observed with the KiTS datasets, where soft mL1-ACE (sL1-ACE) exhibits an increased macro-ECE over baseline, and worse micro-averaged calibration performance compared to hard mL1-ACE (hL1-ACE). However, this departure of the KiTS dataset from the overall trend is corrected when we evaluate the model on a version of the testing dataset that only contains cases with no missing classes. The radar plot in this case is shown in the rightmost column of Fig. 3, where the soft-binned mL1-ACE outperforms the baseline and hard-binned variant for both macro- and micro-average calibration metrics. The presence of missing classes, also occurs for the AMOS and BraTS datasets. When evaluating the models on the testing datasets with no missing classes, we observe a slight uplift in DSC performance of all models, however, it does not significantly change the relative calibration performance of the models, and ECE still shows limited improvements using mL1-ACE auxiliary losses.

5.3 Dataset Reliability Histograms

The observed improvements in calibration resulting from the inclusion of auxiliary mL1-ACE losses are further supported by the dataset reliability histograms in Fig. 4. These histograms show a narrowing of the distribution of predicted probabilities towards the true class frequency, indicating improved calibration, across all datasets, with the greatest improvement resulting from the use of soft-binned mL1-ACE.

5.4 Segmentation Probability Maps

We visualise the resultant probability maps from the models trained with the baseline and mL1-ACE losses in Fig. 5, for a given case and class from the testing dataset. These maps show the predicted foreground probability for each voxel for a given slice, with contours overlaid to show the relationship between the discrete prediction and the ground truth. We observe that the mL1-ACE losses result in a more diffuse probability distribution, with a softening of the class probabilities towards the decision boundary for the false positive (yellow) and particularly the false negative (red) regions of the segmentation. This indicates that the mL1-ACE losses are able to improve the calibration of the models, reducing the overconfidence in the model predictions.

Table 1: Table showing the Dice Similarity Coefficient (DSC) and Average Calibration Error (ACE) metrics with macro- and micro-averaging for the baseline, hard mL1-ACE, and soft mL1-ACE loss function models across four testing datasets. Values show the average class metric, with BraTS and KiTS evaluated on the hierarchical class structure. Values in bold indicate the best performance for each dataset. Asterisks denote significance levels relative to the baseline: * $p < 0.05$, ** $p < 0.01$ (no symbol: non-significant). Standard deviation and statistical significance is not reported for micro-ACE as only one value is available for each dataset.

Loss Function	Dataset	DSC \uparrow	Macro-ACE \downarrow	Micro-ACE \downarrow
Baseline	ACDC 17	0.880 \pm 0.043	0.131 \pm 0.030	0.103
	AMOS 22	0.883 \pm 0.044	0.107 \pm 0.025	0.060
	BraTS 21	0.905 \pm 0.107	0.146 \pm 0.070	0.060
	KiTS 23	0.859 \pm 0.144	0.171 \pm 0.077	0.110
Hard mL1-ACE	ACDC 17	0.880 \pm 0.035	0.102 \pm 0.032**	0.069
	AMOS 22	0.881 \pm 0.047*	0.103 \pm 0.027*	0.052
	BraTS 21	0.905 \pm 0.112	0.132 \pm 0.064**	0.050
	KiTS 23	0.863 \pm 0.131	0.131 \pm 0.066**	0.046
Soft mL1-ACE	ACDC 17	0.871 \pm 0.042**	0.078 \pm 0.030**	0.035
	AMOS 22	0.879 \pm 0.043**	0.087 \pm 0.022**	0.029
	BraTS 21	0.888 \pm 0.127**	0.102 \pm 0.060**	0.025
	KiTS 23	0.860 \pm 0.130	0.109 \pm 0.068**	0.085

6 Discussion and Conclusions

6.1 Limitations of Expected Calibration Error

While Expected Calibration Error (ECE) has been widely adopted as a metric for assessing calibration performance, our work highlights several limitations of relying on ECE as a singular measure. In particular, ECE is heavily influenced by the distribution of counts in each bin, with the first and last bins often being overrepresented when using modern DNNs, as shown in Fig. 1. As a result, ECE tends to be insensitive to the few but clinically relevant errors that modern deep neural networks make, a limitation that becomes especially pronounced in semantic segmentation tasks, where the output space consists of a large number of probability estimates. This issue is further exacerbated in 3D segmentation, such as in medical imaging applications where images can contain over 10^8 voxels, with most of it belonging to the background class. To address these challenges, we propose the use of Average Calibration Error (ACE) as a more robust alternative. Unlike ECE, ACE weights all bins equally, thereby offering more pronounced calibration near the decision boundary (0.5). Although Maximum Calibration Error (MCE) provides insight into the worst-case scenario across bins, our observations indicate that MCE and ACE are highly correlated, supporting the use of ACE as a reliable calibration metric.

6.2 Micro- versus Macro-averaging

Our analysis reveals that micro-averaged calibration errors are consistently lower than their macro-averaged counterparts. This outcome is expected as micro-averaging aggregates binning data across all cases, allowing for miscalibration errors from different inputs to cancel each other out for a given bin.

Although it remains an open question as to whether macro- or micro-averaging is more appropriate for semantic segmentation tasks, we report both metrics to align with established practices in the classification literature where micro-averaging is used. Importantly, we find that the improvements in calibration achieved through our auxiliary calibration losses are more pronounced when assessed with micro-averaged metrics, despite their formulation essentially being macro-averaging.

6.3 Presence of Missing Ground Truth Classes

Another critical observation is the significant impact that images with missing ground truth classes can have on calibration performance. During both training and evaluation, the inclusion of cases with missing classes tends to skew image-level calibration error metrics, leading to an apparent decrease in calibration improvement. By excluding missing classes from the calibration error computation during training, as we have presented here, a more consistent improvement in calibration performance is observed. Similarly, by limiting evaluation to cases with full ground truth classes we observe a more consistent improvement in calibration metrics, however, for completeness we primarily report results on the entire testing dataset. The softening of probability distributions towards the decision boundary, an effect induced by our auxiliary losses, can inadvertently penalise predictions when a class is entirely absent. This observation represents a limitation of our method and suggests that the utility of these auxiliary losses may be reduced in scenarios where missing classes are prevalent. Although this issue is not specific for our calibration losses, as it is also shown to affect Dice loss [41].

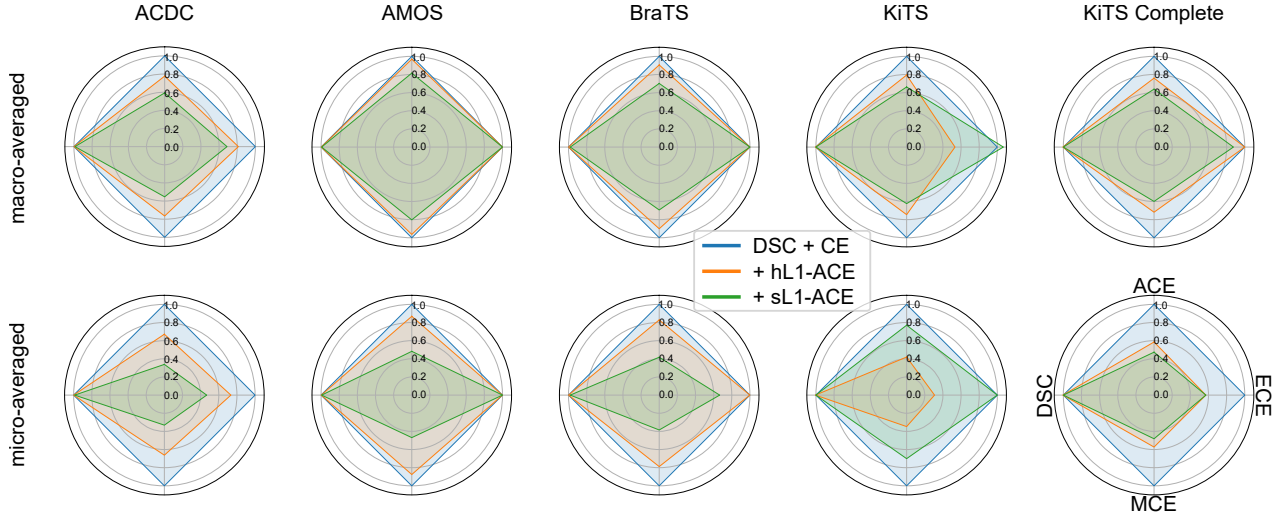


Figure 3: Normalised radar plots showing DSC, ACE, ECE and MCE across the four testing datasets and, in the rightmost column, for the KiTS testing dataset excluding cases with missing classes, keeping only complete cases. Models were trained with three different losses. Blue: baseline (DSC + CE), Orange: baseline plus hard-binned mL1-ACE (hL1-ACE), Green: baseline plus soft-binned L1-ACE (sL1-ACE).

6.4 Comparison of Hard and Soft Binning

When comparing the hard- and soft-binned calibration losses, our results indicate that the soft-binned variant generally delivers superior calibration performance. However, this improvement in calibration comes at a cost: soft binning results in a statistically significant reduction in segmentation performance, as measured by the Dice score, across all datasets except KiTS. This trade-off between calibration and segmentation performance is most pronounced with the soft-binned approach. Conversely, the hard-binned calibration loss maintains segmentation performance comparable to the baseline, with the exception of a modest 0.2% decrease in Dice score for the AMOS 22 dataset, suggesting that it may be more appropriate in applications where segmentation accuracy is paramount.

6.5 Limitations of Calibration Losses

Although our auxiliary calibration losses lead to marked improvements in calibration metrics, it remains to be demonstrated that these gains translate to better clinical outcomes. It is perhaps not surprising that losses based on established calibration metrics would improve those metrics during evaluation. However, our approach is notable for allowing these metrics to be computed at an image level and directly incorporating these as auxiliary losses in a semantic segmentation context. This strategy leverages the large capacity of deep neural networks to learn better-calibrated predictions while exerting only limited negative effects on segmentation performance. It is important to emphasise that our comparisons are made against a baseline loss comprising both DSC and cross-entropy (CE), with the latter generally producing better-calibrated results. In contrast, our previous work relied on a DSC loss as a comparator, which yields highly miscalibrated predictions.

One inherent limitation of our current method is that the process of binning foreground probabilities strips away spatial information, thereby limiting the model’s ability to capture spatial correlations in uncertainty and confidence. Although the visualisations in Fig. 5 demonstrate instances where improvements in calibration align with error regions, this correspondence is not consistent across all cases.

6.6 Conclusion

In this study, we introduced differentiable formulations of marginal L1 Average Calibration Error (mL1-ACE) as auxiliary losses specifically designed for improving the calibration of deep neural networks in medical image segmentation tasks. Through comprehensive evaluations on four publicly available datasets (ACDC, AMOS, BraTS, KiTS), we demonstrated that integrating calibration-aware losses at training time significantly reduces calibration errors, as evidenced by substantial improvements in both macro- and micro-averaged ACE and MCE metrics. The soft-binned mL1-ACE variant provided the largest calibration improvements, reducing macro- and micro-averaged ACE by, an average of, 32% and 48%, respectively, at a small cost in segmentation accuracy (-0.9% DSC). In contrast, the hard-binned variant maintained segmentation accuracy (+0.06% DSC) while reducing macro- and micro-averaged ACE by 16% and 35%, respectively.

Our analysis also highlights limitations in standard calibration metrics, such as Expected Calibration Error (ECE), advocating instead for the use of Average Calibration Error (ACE) to better capture miscalibration, particularly in boundary regions critical to clinical decision-making. Additionally, we introduced dataset reliability histograms, providing intuitive visual insights into calibration performance across entire

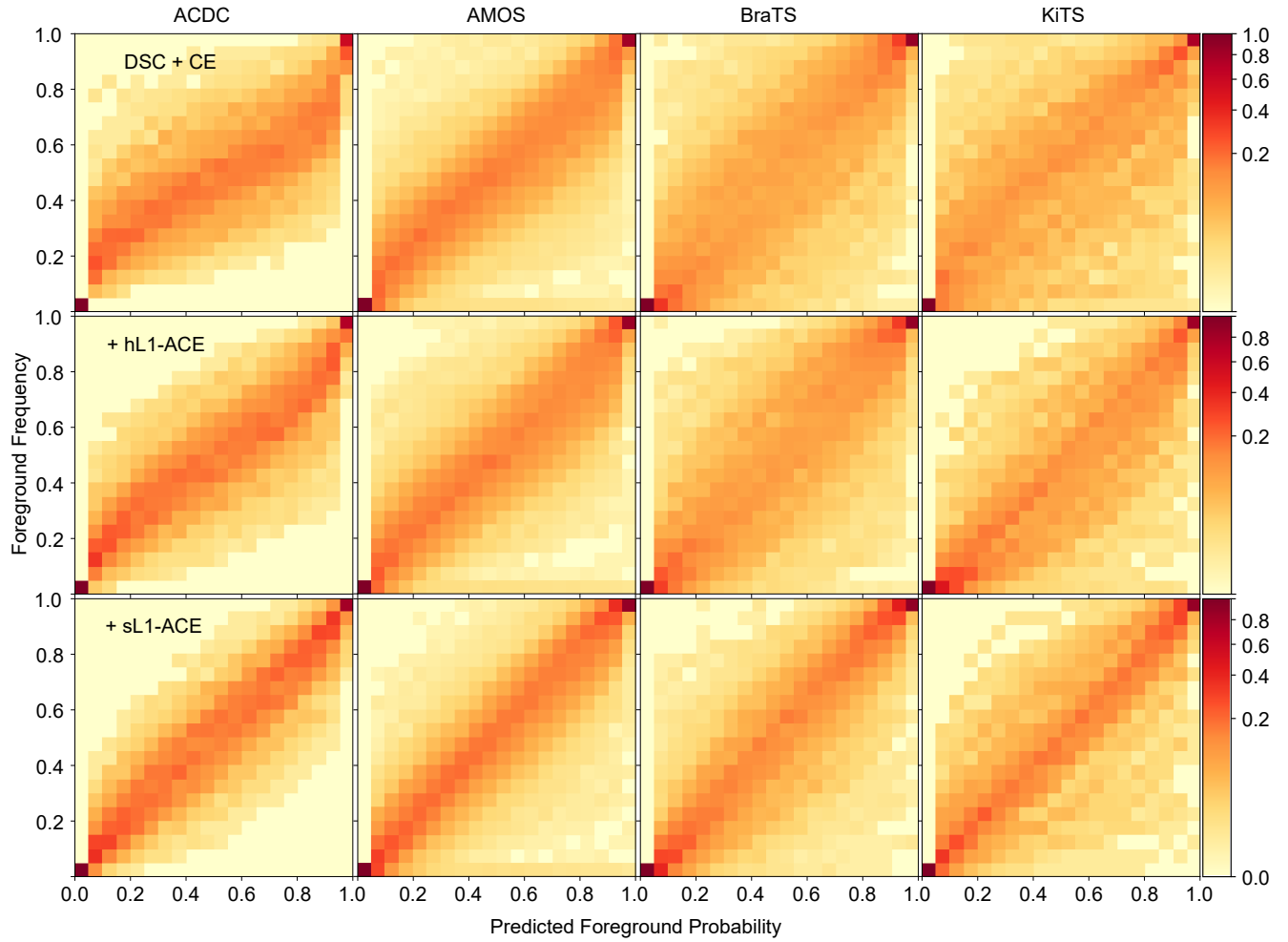


Figure 4: Dataset reliability histograms averaged over classes from each dataset, for baseline loss (DSC + CE) and baseline plus mL1-ACE with hard (hL1-ACE) and soft (sL1-ACE) binning. Gamma correction is applied to the histograms for better visualisation of lower frequencies.

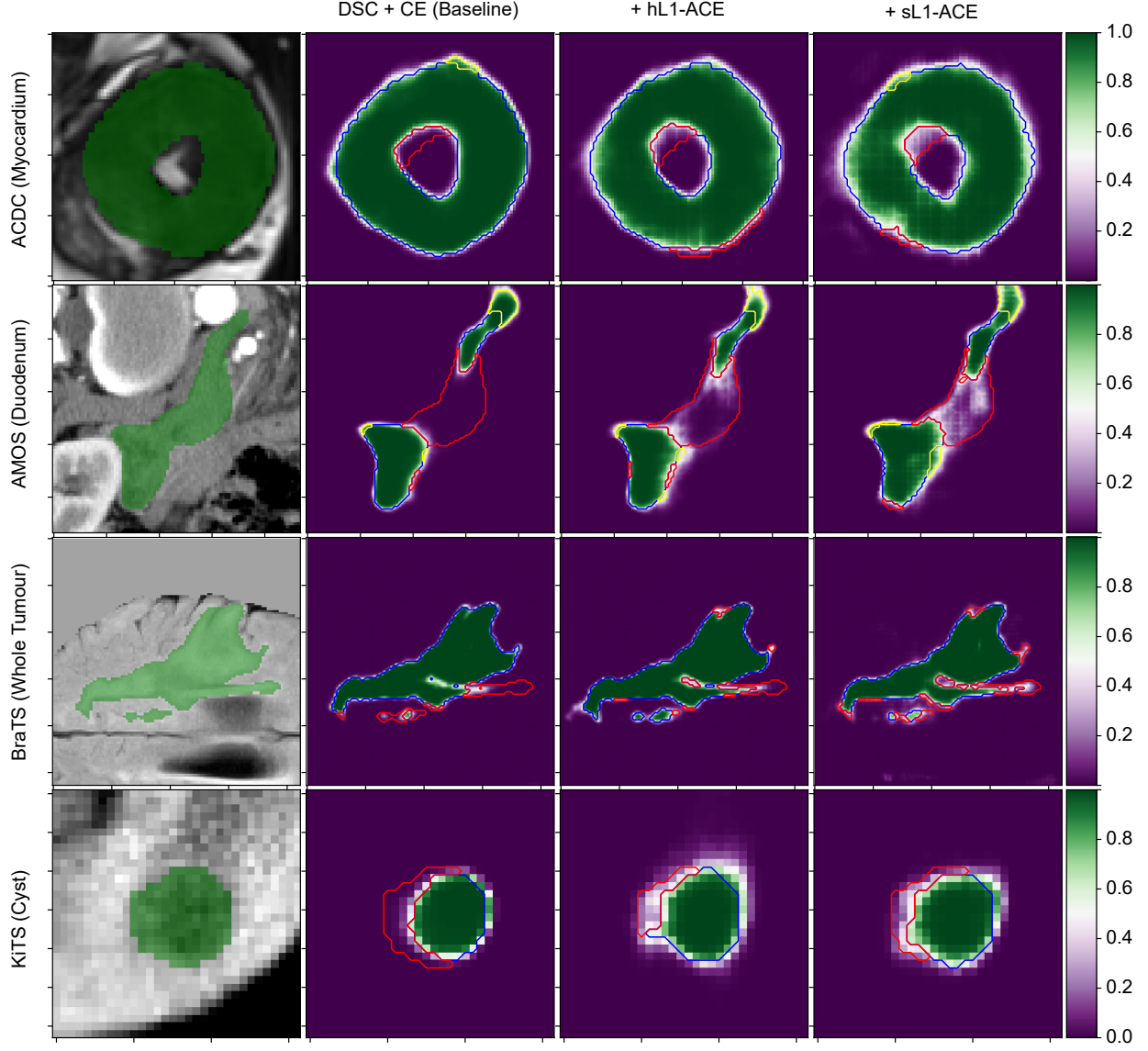


Figure 5: Comparison of predicted segmentation probability maps between baseline and models trained with our auxiliary calibration losses. The leftmost column shows input images with ground truth segmentations. Rows represent different anatomical classes from selected dataset cases. Overlaid contours highlight prediction alignment with ground truth: true positives in blue, false negatives in red, and false positives in yellow.

datasets.

Despite these advances, we identified challenges posed by images with missing ground-truth classes in datasets, suggesting future directions towards more robust handling of such scenarios. Overall, our findings underscore the importance and feasibility of directly optimising for calibration during training, contributing significantly to the development of more reliable and trustworthy medical imaging AI systems suitable for clinical integration.

Acknowledgments

This work was supported by EPSRC CDT [EP/S022104/1], Intel, Medtronic/RAEng [RCSR1819\7\34], and Wellcome/EPSRC [WT203148/Z/16/Z; NS/A000049/1]

References

- [1] Murat Seckin Ayhan and Philipp Berens. Test-time data augmentation for estimation of heteroscedastic aleatoric uncertainty in deep neural networks. In *Proc. Med. Imaging Deep Learn.*, 2018.
- [2] Ujjwal Baid et al. The rsna-asnr-miccai brats 2021 benchmark on brain tumor segmentation and radiogenomic classification. *arXiv preprint arXiv:2107.02314*, 2021.
- [3] T. Barfoot, L. C. Garcia Peraza Herrera, B. Glocker, and T. Vercauteren. Average calibration error: A differentiable loss for improved reliability in image segmentation. In *Medical Image Computing and Computer Assisted Intervention – MICCAI 2024*, pages 139–149, Cham, 2024. Springer Nature Switzerland.
- [4] Christian F. Baumgartner et al. Phiseg: Capturing uncertainty in medical image segmentation. In *Medical Image Computing and Computer Assisted Intervention – MICCAI 2019*, pages 119–127. Springer Int. Publ., 2019.
- [5] Olivier Bernard et al. Deep learning techniques for automatic mri cardiac multi-structures segmentation and diagnosis: Is the problem solved? *IEEE Trans. Med. Imaging*, 37(11):2514–2525, Nov. 2018.
- [6] David Bernstein, Alexandra Taylor, Simeon Nill, and Uwe Oelfke. New target volume delineation and PTV strategies to further personalise radiotherapy. *Phys. Med. Biol.*, 66(5):055024, Feb. 2021.
- [7] Ondrej Bohdal, Yongxin Yang, and Timothy Hospedales. Meta-calibration: Learning model calibration using differentiable expected calibration error. In *Trans. Mach. Learn. Res.*, 2023.
- [8] G. W. Brier. Verification of forecasts expressed in terms of probability. *Mon. Weather Rev.*, 78(1):1–3, Jan. 1950.
- [9] M. Jorge Cardoso et al. MONAI: An open-source framework for deep learning in healthcare. *arXiv*, November 2022.
- [10] Tareen Dawood et al. Uncertainty aware training to improve deep learning model calibration for classification of cardiac mr images. *Med. Image Anal.*, 88:102861, 2023.
- [11] Morris H DeGroot and Stephen E Fienberg. The comparison and evaluation of forecasters. *Journal of the Royal Statistical Society. Series D (The Statistician)*, 32(1/2):12–22, 1983.
- [12] Lucas Fidon, Suprosanna Shit, Ivan Ezhov, Johannes C. Paetzold, Sébastien Ourselin, and Tom Vercauteren. Generalized wasserstein dice loss, test-time augmentation, and transformers for the brats 2021 challenge. In *Brainlesion: Glioma, Multiple Sclerosis, Stroke and Traumatic Brain Injuries*, pages 187–196, Cham, 2022. Springer International Publishing.
- [13] Yarin Gal and Zoubin Ghahramani. Dropout as a bayesian approximation: Representing model uncertainty in deep learning. In *Proc. 33rd Int. Conf. Mach. Learn.*, volume 48, pages 1050–1059. PMLR, 2016.
- [14] Chuan Guo, Geoff Pleiss, Yu Sun, and Kilian Q. Weinberger. On calibration of modern neural networks. In *Proc. 34th Int. Conf. on Machine Learning*, volume 70 of *Proc. Machine Learning Research*, pages 1321–1330. PMLR, Aug. 2017.
- [15] Ramya Hebbalaguppe, Jatin Prakash, Neelabh Madan, and Chetan Arora. A stitch in time saves nine: A train-time regularizing loss for improved neural network calibration. In *Proc. 2022 IEEE/CVF Conf. Comput. Vis. Pattern Recognit. (CVPR)*, pages 16060–16069, 2022.
- [16] Nicholas Heller et al. The state of the art in kidney and kidney tumor segmentation in contrast-enhanced ct imaging: Results of the kits19 challenge. *Med. Image Anal.*, 67:101821, 2021.
- [17] Fabian Isensee et al. nnu-net revisited: A call for rigorous validation in 3d medical image segmentation. In *Medical Image Computing and Computer-Assisted Intervention – MICCAI 2024*, pages 488–498, Cham, 2024. Springer Nature Switzerland.
- [18] Yuanfeng Ji et al. Amos: A large-scale abdominal multi-organ benchmark for versatile medical image segmentation. In *Adv. Neural Inf. Process. Syst.*, volume 35, pages 36722–36732. Curran Associates, Inc., 2022.
- [19] Archit Karandikar et al. Soft calibration objectives for neural networks. In *Adv. Neural Inf. Process. Syst.*, volume 34, pages 29768–29779. Curran Associates, 2021.
- [20] Alex Kendall and Yarin Gal. What uncertainties do we need in bayesian deep learning for computer vision? In

- Adv. Neural Inf. Process. Syst.*, volume 30, pages 5574–5584. Curran Assoc., Inc., 2017.
- [21] Simon Kohl, Bernardino Romera-Paredes, Clemens Meyer, Jeffrey De Fauw, Joseph R. Ledsam, Klaus Maier-Hein, S. M. Ali Eslami, Danilo Jimenez Rezende, and Olaf Ronneberger. A probabilistic u-net for segmentation of ambiguous images. In *Adv. Neural Inf. Process. Syst.*, volume 31, pages 6965–6975. Curran Assoc., Inc., 2018.
 - [22] Ranganath Krishnan and Omesh Tickoo. Improving model calibration with accuracy versus uncertainty optimization. In *Adv. Neural Inf. Process. Syst.*, volume 33, pages 18237–18248. Curran Assoc., Inc., 2020.
 - [23] Aviral Kumar, Sunita Sarawagi, and Ujjwal Jain. Trainable calibration measures for neural networks from kernel mean embeddings. In *Proc. 35th Int. Conf. on Machine Learning*, volume 80, pages 2805–2814. PMLR, 2018.
 - [24] Balaji Lakshminarayanan, Alexander Pritzel, and Charles Blundell. Simple and scalable predictive uncertainty estimation using deep ensembles. In *Adv. Neural Inf. Process. Syst.*, volume 30, pages 6402–6413. Curran Assoc., Inc., 2017.
 - [25] Gongbo Liang, Yu Zhang, Xiaoqin Wang, and Nathan Jacobs. Improved trainable calibration method for neural networks on medical imaging classification. In *British Machine Vision Conference (BMVC)*, 2020.
 - [26] Jun Ma et al. Loss odyssey in medical image segmentation. *Med. Image Anal.*, 71:102035, 2021.
 - [27] Alireza Mehrtash, William M. Wells, Clare M. Tempany, Purang Abolmaesumi, and Tina Kapur. Confidence calibration and predictive uncertainty estimation for deep medical image segmentation. *IEEE Trans. Med. Imaging*, 39(12):3868–3878, Dec. 2020.
 - [28] Raghav Mehta et al. Qu-brats: Miccai brats 2020 challenge on quantifying uncertainty in brain tumor segmentation – analysis of ranking scores and benchmarking results. *Mach. Learn. Biomed. Imaging*, 1(August 2022 issue):1–54, 2022.
 - [29] Miguel Monteiro et al. Stochastic segmentation networks: Modelling spatially correlated aleatoric uncertainty. In *Adv. Neural Inf. Process. Syst.*, volume 33, pages 12756–12767. Curran Assoc., Inc., 2020.
 - [30] Balamurali Murugesan, Sukesh Adiga Vasudeva, Bingyuan Liu, Herve Lombaert, Ismail Ben Ayed, and Jose Dolz. Trust your neighbours: Penalty-based constraints for model calibration. In *Medical Image Computing and Computer Assisted Intervention – MICCAI 2023*, pages 572–581, Cham, 2023. Springer Nature Switzerland.
 - [31] Balamurali Murugesan, Sukesh Adiga Vasudeva, Bingyuan Liu, Herve Lombaert, Ismail Ben Ayed, and Jose Dolz. Neighbor-aware calibration of segmentation networks with penalty-based constraints. *Med. Image Anal.*, 101:103501, 2025.
 - [32] Andriy Myronenko. 3d mri brain tumor segmentation using autoencoder regularization. In *Brainlesion: Glioma, Multiple Sclerosis, Stroke and Traumatic Brain Injuries*, pages 311–320, Cham, Switzerland, 2019. Springer International Publishing.
 - [33] Andriy Myronenko, Dong Yang, Yufan He, and Daguang Xu. Automated 3d segmentation of kidneys and tumors in miccai kits 2023 challenge. In *Kidney and Kidney Tumor Segmentation*, pages 1–7, Cham, Switzerland, 2024. Springer Nature Switzerland.
 - [34] Lukas Neumann, Andrew Zisserman, and Andrea Vedaldi. Relaxed softmax: efficient confidence auto-calibration for safe pedestrian detection. In *2018 NIPS MLITS Workshop: Machine Learning for Intelligent Transportation System*. OpenReview, 2018.
 - [35] Mahdi Pakdaman Naeini, Gregory Cooper, and Milos Hauskrecht. Obtaining well calibrated probabilities using bayesian binning. *Proc. AAAI Conf. Artif. Intell.*, 29(1), Feb. 2015.
 - [36] John Platt. Probabilistic outputs for support vector machines and comparisons to regularized likelihood methods. *Advances in Large Margin Classifiers*, 10(3):61–74, 1999.
 - [37] Teodora Popordanoska, Raphael Sayer, and Matthew Blaschko. A consistent and differentiable lp canonical calibration error estimator. In *Adv. Neural Inf. Process. Syst.*, volume 35, pages 7933–7946. Curran Assoc., Inc., 2022.
 - [38] Axel-Jan Rousseau, Thijs Becker, Simon Appeltans, Matthew Blaschko, and Dirk Valkenburg. Post hoc calibration of medical segmentation models. *Discov. Appl. Sci.*, 7(3):180, 2025.
 - [39] Christian Szegedy, Vincent Vanhoucke, Sergey Ioffe, Jon Shlens, and Zbigniew Wojna. Rethinking the inception architecture for computer vision. In *2016 IEEE Conference on Computer Vision and Pattern Recognition (CVPR)*, pages 2818–2826. IEEE, 2016.
 - [40] Sunil Thulasidasan, Gopinath Chennupati, Jeff A Bilmes, Tanmoy Bhattacharya, and Sarah Michalak. On mixup training: Improved calibration and predictive uncertainty for deep neural networks. In *Adv. Neural Inf. Process. Syst.*, volume 32. Curran Associates, Inc., 2019.
 - [41] Sofie Tilborghs, Jeroen Bertels, David Robben, Dirk Vandermeulen, and Frederik Maes. The dice loss in the context of missing or empty labels: Introducing ϕ and ϵ .

In *Medical Image Computing and Computer Assisted Intervention – MICCAI 2022*, pages 527–537, Cham, 2022. Springer.

- [42] Michael Yeung, Leonardo Rundo, Yang Nan, Evis Sala, Carola-Bibiane Schönlieb, and Guang Yang. Calibrating the dice loss to handle neural network overconfidence for biomedical image segmentation. *J. Digit. Imaging*, 36(2):739–752, Apr. 2023.
- [43] Hongyi Zhang, Moustapha Cisse, Yann N. Dauphin, and David Lopez-Paz. mixup: Beyond empirical risk minimization. In *International Conference on Learning Representations (ICLR)*, 2018.